Effects of $NiCl_2$ and $FeCl_2$ additives on the anodic dissolution behaviours of Inconel 600 in molten LiCl–KCl salts

Younghwan Jeon, Jungho Hur, Gwan Yoon Jeong, Seungmin Ohk, Jaeyeong Park

PII: S0010-938X(23)00184-1
DOI: https://doi.org/10.1016/j.corsci.2023.111142
Reference: CS111142

To appear in: *Corrosion Science*

Received date: 18 December 2022
Revised date: 26 February 2023
Accepted date: 24 March 2023

Please cite this article as: Younghwan Jeon, Jungho Hur, Gwan Yoon Jeong, Seungmin Ohk and Jaeyeong Park, Effects of $NiCl_2$ and $FeCl_2$ additives on the anodic dissolution behaviours of Inconel 600 in molten LiCl–KCl salts, *Corrosion Science,* (2023) doi:https://doi.org/10.1016/j.corsci.2023.111142

Effects of $NiCl_2$ and $FeCl_2$ additives on the anodic dissolution behaviours of Inconel 600 in molten LiCl–KCl salts

Younghwan Jeon[a], Jungho Hur[a], Gwan Yoon Jeong[b], Seungmin Ohk[a], Jaeyeong Park[a,*]

[a]Department of Nuclear Engineering, Ulsan National Institute of Science and Technology, 50 UNIST-gil, Ulju-gun, Ulsan 44919, Republic of Korea

[b]Korea Atomic Energy Research Institute, 989-111 Daedeok-daero, Yuseong-gu, Daejeon 34057, Republic of Korea

[*]Corresponding author: Jaeyeong Park, E-mail: jypark@unist.ac.kr

Abstract

The anodic dissolution behaviour of Inconel 600 must be elucidated to design an efficient decontamination process for used nuclear steam generator tubes with radioactive nuclide depositions in their surface microcracks. We investigated the effects of $NiCl_2$ and $FeCl_2$ additives in LiCl–KCl eutectic salts on the microstructural changes in Inconel 600 during electrolytic decontamination. A Cr–Fe depletion layer formed on Inconel 600 via Ni reduction at the position where alloying elements oxidised. In the $FeCl_2$-added salt, the selective dissolution of active alloying elements through the grain boundary produced a cavity-cluster layer whose shape was changed using applied electrochemical methods.

Keywords: Nickel alloy (A); Molten salt (A); Anodic dissolution (C); Microparticle recovery (B); SEM−EDS (B)

1. Introduction

Inconel 600, a nickel-based alloy containing 14%–17% chromium, 6%–10% iron, and trace elements such as C, Mn, S, Si, and Co, is widely used in industries employing harsh environments, owing to its high strength and high-temperature corrosion resistance. The alloy is used for fabricating steam generator tubes for pressurised water reactors (PWRs); however, stress corrosion cracking (SCC) can accelerate the degradation of these tubes [1-6]. Used PWR steam generator tubes are classified as very-low-level or low-level radioactive wastes based on the radioactive contaminants (e.g., Co-60, Cs-137, and other fission products) absorbed on their inner surfaces and cracks. However, because the base alloy is not exposed to neutron-irradiation environments, the used tubes may be recycled after appropriate surface decontamination treatment, depending on the crack and contamination characteristics [7-9].

Decontamination techniques based on physical abrasives and chemicals are commonly employed to treat surfaces contaminated with metallic radioactive wastes [10-14]; however, they are unsuitable for complexly shaped steam generator tubes, with diameters, thicknesses, and lengths of 10 mm, 1 mm, and 4–8 m, respectively. Although solution-based chemical decontamination techniques are well developed for various structural materials, even those with complex shapes [15-18], microcracks on steam generator tubes deeper than 100 μm impede reactions between chemical detergents and radioactive contaminants [19-22]. Studsvik, a company that provides technical services to the nuclear industry, has experience in used steam generators decontamination which was conducted through chemical decontamination followed by polishing. The radioactive doses of the treated tubes, unlike those of other recycled parts [23,24], were still exceedingly high for the disposal of the treated tubes as radioactive wastes.

Electrochemical decontamination processes based on molten salt may be feasible alternatives to those employing physical abrasives and chemicals, as they can manage the dissolution behaviours of the contaminated tubes and improve the recovery processes. In particular, these techniques are advantageous not only for surface decontamination but also for volumetric decontamination [25-27]; further, they can minimise secondary waste by adopting salt purification [28,29], unlike existing commercialised physical and chemical decontamination technologies. Many studies have attempted to control the purities of the products at the cathode in various salt systems [7,30-32]. The operating parameters such as the applied current, applied potential, and the electrolyte composition can cause microstructural changes in the target material during electrochemical dissolution [33-42]; however, the anodic dissolution behaviours of Inconel 600 in molten salt systems have not been analysed. Therefore, to verify the feasibility and efficiency of molten-salt-based electrochemical decontamination, the anodic dissolution behaviours of Inconel 600 must be investigated in a molten-chloride-salt system. This would enable the design of a radioactively contaminated steam generator tube decontamination process (Fig. S1 and Fig. S2) by reference to other papers proposing decontamination processes for the structural materials of molten-salt-based nuclear power plants.

In this study, we examined the anodic dissolution behaviours of Inconel 600 in LiCl–KCl–5-wt.%-$NiCl_2$/$FeCl_2$ at 773 K. Using scanning electron microscopy coupled with energy-dispersive X-ray spectroscopy (SEM–EDS), we investigated the microstructural changes in Inconel 600 arising from the application of various anodic potentials or current densities and the microparticles that detached from it during electrochemical treatment. The contents of Cr, Fe, and Ni in the molten salts were measured through an electrochemical experiment and subsequent inductively coupled plasma–optical emission spectrometry (ICP–OES) to analyse the behaviours of the electrolytes during the process. In addition, the anodic dissolution behaviours of Inconel 600 were studied in molten LiCl–KCl eutectic salts with Ni and Fe chloride additives, via potential and current density changes at the electrodes, and changes in the salt contents.

2. Experimental

2.1. Electrochemical cell

Anhydrous LiCl–KCl powder of a eutectic composition (Alfa Aesar, 99.99%); anhydrous $NiCl_2$ (Alfa Aesar, 99.99%); and anhydrous $FeCl_2$ (Alfa Aesar, 99.99%) were heated for 48 h at 473 K in a globe box to eliminate residual moisture. The resulting mixture was melted and solidified as a salt chunk to minimise the measurement error caused by the adhesion between the salt and cell. The compositions of five randomly selected samples of the solidified chunk were analysed via ICP–OES (700-ES, Agilent, USA), and the contents of $NiCl_2$ and $FeCl_2$ were determined to be 5.0360 ± 0.0241 and 5.0158 ± 0.0393 wt.%, respectively. The subsequent electrochemical experiments were conducted using 30.000 g of the salts, which were measured using an electronic microbalance with a resolution of 10^{-5} g.

The electrochemical experiments and preparation of the reagents/specimen were conducted in a glove box filled with Ar gas (99.996%), whose oxygen and moisture concentrations were maintained under 0.1 ppm. The temperature was controlled between ±0.5 °C, using an electrical furnace attached to the bottom of the glove box and a proportional integral derivative (PID) controller. As shown in Fig. 1, a Pyrex tube, with an inner diameter of 32 mm and a height of 370 mm, was used to hold the molten salt electrolytes. Specifically, the bottom of the tube was split to prevent intermixing of the particles detached from the anode and cathode. Their separation was confirmed by analysing the recovered particles on each side (Fig. S3-5). Before the electrochemical experiment, a dummy cell was filled with 30.000 g of the LiCl–KCl salt, and a K-type thermocouple with a Teflon plug was installed to determine the temperature of the furnace. To indirectly obtain reliable temperature measurements, the Teflon plug was also used as a holder to ensure that the electrodes were steady. Simple immersion experiments (Table 1. NI-1, 2 and FI) were conducted in the same glove box/furnace system; however, a differently sized Pyrex tube, with an inner diameter of 13 mm, was used. Salts containing 3.000 g of LiCl–KCl–5-wt.%-$NiCl_2$/$FeCl_2$ were used for each experiment, and the immersed specimen was the same as the anode of the electrochemical experiment.

Inconel 600 (Special metals, USA) which was used as the anode (Fig. 1, green part) was machined using a laser cutter (K2CMS1, K2 laser system, Republic of Korea) with a 5 μm tolerance and polished using a 1200-grit sandpaper to remove the oxide layer and residual effects induced by the cutting procedure on the surface and flatten it. A reacting section, with dimensions of 10 × 15 × 1 mm^3 (total area: 3.48 cm^2), was designed to be immersed in the molten salt; further, a 2-millimetre-wide connecting section was used to minimise the error in surface area caused by a change in the immersion depth (1.72 reacting section area% mm^{-1}). The average grain size of the Inconel 600 specimen was evaluated as 15.2 μm using electron backscattering diffraction (EBSD). Three holes, each with a diameter of 1 mm, in the holder above the connecting section were used to fasten a piece of iron wire (Alfa Aesar, 99.998%) to the anode. A 1-millimetre-wide, 6-millimetre-long top joint was inserted in a Pyrex guide tube with a diameter of 2 mm to ensure immobility of the anode.

Two tungsten rods (Alfa Aesar, 99.996%), each with a diameter of 4.0 mm, were used as the cathode. The immersed depth of the cathode was set to 20 mm (5.03 cm^{-2}) to prevent the current-limitation phenomenon, whereby an insufficient cathode surface area results in insufficient electron transfer as well as an inadequately distorted anode potential or current density and fewer reducing ions (Ni^{2+} and Fe^{2+} for the $NiCl_2$ and $FeCl_2$ additives, respectively). A Ag/AgCl electrode, composed of LiCl–KCl–1-wt.%-AgCl (Sigma Aldrich, 99.999%) and Ag wire (Alfa Aesar, 99.999%) with a diameter of 1.0 mm, was inserted into a Pyrex tube, whose tip thickness was less than 0.5 mm, and used as a reference electrode to establish ionic conduction. The AgCl content in the LiCl–KCl–AgCl salt was determined to be 1.000 ± 0.010 wt.% via ICP–OES. Thereafter, the Ag wire was polished using 800-grit sandpaper, rinsed with 70% nitric acid for 30 s to remove any impurities, and cleaned with distilled water to remove silver nitrate.

2.2. Detached-particle recovery system

A microparticle-recovery system was designed to retrieve microparticles detached from the anode during anodic dissolution (Fig. 2). By applying negative pressure through this system, which was installed inside the furnace connected with the glove box, microparticles in the molten salt were sieved through a microfiber. After anodic dissolution, the salt that had solidified on the anode side (Fig. S5) was placed on an iron hopper (Fig. 2 green part), and the temperature was increased to 673 K, which is higher than the melting temperature of eutectic LiCl–KCl (628 K). To prevent tearing of the microparticles owing to a large pressure gradient, 1 kPa, which was the lowest pressure drop supported by the system, was applied to separate the microparticles from the molten salt.

At a filter pore size significantly smaller than the microparticle size, the particles blocked the micropores and restricted salt flow, resulting in insufficient removal of the remaining salt from the particles and disruption in the collection of the microparticles to be examined.

Therefore, the appropriate pore size was determined based on the microparticle size. For the microfilters, Grade-D and Grade-F microfibers (Sterlitech, USA) fabricated using borosilicate glass, with pore sizes of 2.7 and 0.7 μm, respectively, were selected via preliminary parametric studies on the relation between filter pore sizes and microparticle sizes. Grade-D and Grade-F microfibers were used to recover the microparticles from the $NiCl_2$- and $FeCl_2$-additive experiments, respectively.

2.3. Experimental procedures

The immersion experiments were conducted to determine the microstructural changes in the Inconel 600 immersed in LiCl–KCl–5-wt.%-$NiCl_2$/$FeCl_2$ at 773 K (i) without any electrochemical application (Table 1: NI and FI) and (ii) with potentiostatic or galvanostatic electrochemical application (Table 1: NP, NG, FP, and FG). Two potentiostats (VersaSTAT3F and VersaSTAT3) and VersaStudio software (AMETEK SI, UK) were used for the electrochemical experiments. One potentiostat was used to construct a three-electrode cell consisting of Inconel as the working electrode (anode), W rods as the counter electrode (cathode), and Ag/AgCl electrode as the reference electrode. The other potentiostat was used to measure the potential of the counter electrode at the same time.

Immersion tests employing the $NiCl_2$ and $FeCl_2$ additives (NI and FI) were conducted to determine the chemical reaction between Inconel 600 and the additive ions when the specimen was immersed in LiCl–KCl–5-wt.%-$NiCl_2$/$FeCl_2$ molten salts. The applied potentials in the potentiostatic experiments were set in a manner that prevented the reduction of the Ni^{2+} or Fe^{2+} additive ions on the anode. During the preliminary experiments, to establish the experimental conditions for the $NiCl_2$-added salt, the reduction of Ni on the surface of Inconel 600 was observed. However, the anodic current was observed with an applied potential of 0.10 V (vs. Ag/1 wt.% AgCl) which implies that the amount of Ni reduced was smaller than those of Cr and Fe oxidised. However, reduced Ni at a higher amount served as a coating, disrupting the anodic dissolution of Inconel 600. Thus, the applied potential ranges were determined to be 0.15–0.25 and 0.05–0.15 V (vs. Ag/1 wt.% AgCl) for the $NiCl_2$ and $FeCl_2$ additive salts, respectively, to prevent the reduction of additive ions at the anode. For an intuitive comparison between the potentiostatic and galvanostatic experiments, the applied current densities of the galvanostatic experiments were set to 6, 16, and 30 mA cm^{-2}, the average current densities observed during the potentiostatic experiments.

Meanwhile, the anodic dissolution behaviours of Inconel 600 in the $NiCl_2$/$FeCl_2$ additive salts were different, causing a significant difference in the reduced thicknesses of the anode specimens for the charge passed in the presence of various additive salts. Therefore, the charges passed for the $NiCl_2$ and $FeCl_2$ additive salts were set to 1,000 C (287 C cm^{-2}) and 280 C (80 C cm^{-2}), respectively, to (i) induce a sufficient change on the anode surface, (ii) prevent extreme damage to the anode, (iii) increase the number of particles detached from the anode, and (iv) ensure no contact between the anode and reduced substance under the experimental conditions.

Before all the experiments, the electrodes/specimens were heated above the molten salt for >1 h and inserted into it to guarantee the salt stability from thermal shock and quick stabilisation of the electrochemical cell. All electrochemical experiments were conducted within 30 min after the electrode/specimen immersion, and the open-circuit potential change was less than 5 mV h^{-1}. The electrodes were quickly removed after the experiments. Salt solidification was also confirmed quickly by removing the cell from the furnace and collecting the samples for content determination from the central and upper sections of the cell to minimise the influence of the substance detached from the anode and cathode.

The disjoined anode was rinsed thrice with quiescent distilled water to remove adhered salts. The reaction section was split into two parts, which were placed on a graphite mount, polished using 400-grit sandpaper, and finished using a 0.25-micrometre diamond suspension. The microstructural changes in the polished sample were characterised via SEM–EDS (EM-30AX, COXEM, Republic of Korea). Microparticles that had been sieved through a filter were prepared and characterised together using SEM–EDS. ICP–OES was used to analyse the salt content which was collected from the part without any metallic dust throughout all experiments. The relative standard deviation (%RSD) varies between 0.0 and 0.6% when there is more than 0.01 wt.% of the analyte element in the salt.

3. Results

3.1. Corrosion behaviours of Inconel 600 in chloride salts containing Ni and Fe additives (NI and FI)

The Inconel 600 specimens were immersed in the LiCl–KCl–5-wt.%-$NiCl_2$ molten salt for 3 and 168 h and subsequently removed from the cell. Their microstructures were then investigated using SEM–EDS. As shown in Fig. 3 (a-1), (a-2), (b-1), and (b-2), a reduced Ni layer with a thickness of ~3 mm was observed in both specimens. A coarser Ni layer was observed on the surface of the NI specimen immersed for 3 h, whereas a finer Ni layer was observed on the specimen immersed for 168 h. The compositions of the salts indicated that, with increasing time, the Ni content decreased and Cr content increased, whereas the Fe content remained unchanged (Table 2). SEM – EDS was conducted to measure the composition of the surface layer; results indicated that the Ni content was >99.3 wt.%. A concentration gradient was observed for Cr over 1 μm in the thickness direction of the deposited layer, whereas the Fe content remained unchanged.

The Inconel 600 immersed in LiCl–KCl–5-wt.%-FeCl$_2$ for 168 h did not exhibit any distinct surface change (Fig. 3 (c)). Unlike the Ni layer in the NI experiment, the Fe layer was not reduced via exposure to the NiCl$_2$ additive. Table 2 lists the major elemental contents in the salts before and after the NI and FI experiments.

3.2. Potentiostatic and galvanostatic anodic dissolution behaviours of Inconel 600 in LiCl–KCl–5-wt.%-NiCl$_2$ at 773 K (NP and NG, respectively)

Figure 4 shows the changes in electrode potentials and anode current densities with time in the NP and NG experiments for anodic dissolution. In the NP experiments, the current densities decreased with time but stabilised at higher anode potentials. In the NG experiments, the anode potential increased with time and was 20–60 mV higher than that observed under similar conditions in the NP experiment. The cathode potential was also recorded to confirm the reduction of Cr^{2+} and Fe^{2+} ions during the experiment. Additionally, the Cr, Fe, and Ni contents in the reduced metal were investigated via ICP–OES. The purity of Ni was >99 wt.%, whereas the Cr and Fe contents were <0.0010 wt.% in all cases.

The microstructures of Inconel 600 after the NP and NG experiments were observed using SEM–EDS. and Fig. 5 simultaneously represents the secondary electron images with EDS mapping images. After the NP and NG experiments, a Cr–Fe depletion layer, with the Cr and Fe content lower than that of the base material, was formed on the anode surface. The thicknesses and contents of the Cr–Fe depletion layer, summarised in Table 3, were investigated via SEM–EDS. As presented in Table 3, with increasing applied potential and current density, the thickness of the Cr–Fe depletion layer decreased, whereas the remaining amounts of Cr and Fe increased. The reduced specimen thicknesses, Cr–Fe depletion layer thicknesses, and Cr and Fe contents in the Cr–Fe depletion layers were larger in the NP experiments than in the NG experiments.

Cracks originating from the boundary of the Cr–Fe depletion layer and directing toward the base material were not observed in the NP-1, NP-2, NG-1, and NG-2 experiments; however, specimen NP-3 contained several microcracks oriented toward the thickness direction of the substrate. In the case of NG-3, there were no cracks in the base material; however, numerous cracks vertical to the surface were observed in the Cr–Fe depletion layer.

After the anodic dissolution experiments, the salt contents were analysed via ICP–OES (Table 4). In the NP experiment, the Ni content did not exhibit any clear variation with the applied potential; however, an increase in the applied potential reduced the Cr content and increased the Fe content. By contrast, in the NG experiment, the Cr and Fe contents did not exhibit any clear variation, whereas the Ni content increased with the current density. The Cr and Fe contents were higher and lower, respectively, in the NP experiments than in the NG experiments.

3.3. Potentiostatic and galvanostatic anodic dissolution behaviours of Inconel 600 in LiCl–KCl–5-wt.%-$FeCl_2$ at 773 K (FP and FG, respectively)

FP-1–3 and FG-1–3 experiments were conducted to investigate the anodic dissolution behaviours of Inconel 600 in LiCl–KCl–5-wt.%-$FeCl_2$ using the potentiostatic and galvanostatic methods, respectively. Figure 6 shows the chronoamperograms and chronopotentiograms of the results of the experiments. The current density did not change significantly in the FP-1 experiment; however, it decreased sharply at the beginning of the FP-2 and FP-3 experiments and stabilised thereafter. The anode potential recorded in all FG experiments increased rapidly within the initial 300 s and then stabilised. The anode potentials observed during the FG experiments were higher than those observed during the FP experiments, at least from 30 to 110 mV. After the experiment and after washing the reduced metals with distilled water, their contents were analysed via ICP–OES. The Ni, Cr, and Fe contents were <0.0080, <0.0010, and >90 wt.%, respectively, for all experiments, and the balance of approximately 10 wt.% might be attributable to oxygen from the oxidation caused by washing.

Figure 7 presents the microstructural images of Inconel 600 after the FP and FG experiments. Cluster layers containing several cavities were generated at the surfaces of all specimens. The contents of the cavity-cluster layers, which were investigated via SEM–EDS, are summarised in Table 5, along with their characteristics. The Ni content decreased and the Fe and Cr contents increased with increasing potential or current density; however, these trends were not as significant as those observed in the NP or NG experiments. The charge passed was 80 C cm^{-2}, and the reduced thickness was 150–250 μm, which was significantly higher than that in the NP and NG experiments, even though they employed 280 C cm^{-2} of charge. At the boundary of the base material, cracks shorter than 15 μm were observed.

The cavities in the FP-1 and FP-2 specimens were <5 μm, which is smaller than the grain size of Inconel 600 (20 μm). The cavity size in other experiments was difficult to measure because of their figuration. In particular, the cavities observed in the FP-3 experiments exhibited a rounded shape, which was similar to those observed in the FG experiments. Furthermore, as shown in the red circle in Fig. 7 (c, e, and f), smudged edges were observed in FP-3, FG-2, and FG-3.

The contents of the salts after the FP and FG experiments were analysed via ICP–OES, and the results are summarised in Table 6. After the experiments, the Ni content in the molten salt remained unchanged, whereas the Fe and Cr contents increased. For a passing charge of 280 C, an Fe content of 1.9398% corresponds to the recovery of pure iron at the cathode and dissolution of no element at the anode. From the results, the dissolved amounts of Cr and Fe can be estimated, using the salt contents in Table 6. A χ value, representing the ratio of the amounts of dissolved Cr and Fe, can be defined as follows.

$$\chi = \frac{dissoluted\ amount\ of\ Cr\ (mol\%)}{dissoluted\ amount\ of\ Fe\ (mol\%)} \qquad (1)$$

The χ value decreased with increasing applied potential or current density (Table 6). Essentially, with increasing applied potential or current density, the amount of dissolved Fe increased, whereas that of dissolved Cr decreased. Under similar conditions, the χ values obtained in the FP experiments were more than twice those obtained in the FG experiments.

To study the variation in the surface morphology with the anodic dissolution method in the LiCl–KCl–FeCl$_2$ molten salt, a charge of 1 C cm^{-2}, which is significantly smaller than the previously established 80 C cm^{-2}, was passed at an applied potential of 0.05 V (vs. Ag/1 wt.% AgCl) or an applied current density of 6 mA cm^{-2}. After coulometry, the microstructure of the anode was scanned via SEM (Fig. 8). As shown in Fig. 8 (a), cracks with various orientations (perpendicular or parallel to the substrate) were observed, a few of which split from other cracks. By contrast, the cracks in FG-4, which were significantly thicker but shorter than those in FP-4, exhibited a spread and complex shapes. The edge of FG-4 was rough; however, it macroscopically exhibited a flat surface, whereas that of FP-4 was uneven, as if particles had escaped from it.

3.4. Analysis of the particles detached from the Inconel 600 anode in LiCl–KCl–5-wt.%-$NiCl_2$ and $FeCl_2$ at 773 K

After the anodic dissolution experiments, the solidified salt at the anodic side, which contained particles that had detached from it, was inserted into the microparticle-recovery system (as detailed in section 2.2). Microparticles detached from the anode were captured using the microfilter and characterised via SEM–EDS (Fig. 9). Table 7 summarises the sizes and compositions of the microparticles determined via EDS.

As shown in Fig. 9, the sheet-shaped detached particles from the anodic dissolution experiments conducted on the LiCl–KCl–5-wt.%-$NiCl_2$ molten salt system contained large amounts of relatively small particles. The particle sizes and eliminated amounts of Cr/Fe decreased with increasing applied current density. The Cr and Fe contents in the detached particles were lower than those in the Cr–Fe depletion layer (Table 3).

Small detached particles from the $FeCl_2$ additive salt were stone-shaped. The sizes of the particles negligibly decreased as the applied current density increased. However, the contents of the detached particles were significantly different from those reported in Table 5. As indicated by Table 6 and the Ni content of the reduced complex, only a small amount of Ni, which is the least reactive element in Inconel 600, dissolved. Assuming that Ni did not oxidise during the anodic dissolution experiments on $FeCl_2$-added salt, a δ value representing the dissolution rate can be defined as follows.

$$\delta = 1 - \frac{(Fe\ or\ Cr\ content\ /\ Ni\ content)_{cavity\ cluster\ or\ detached\ particles}}{(Fe\ or\ Cr\ content\ /\ Ni\ content)_{Inconel\ 600}} \qquad (2)$$

A δ value close to 1 indicates that majority of the Cr or Fe had been eliminated from the anode, whereas a value close to 0 indicates that majority of the Cr or Fe had remained in the anode. As indicated by Table 5 and Table 7, the $\delta_{\text{Fe, cavity-cluster}}$, $\delta_{\text{Fe detached particles}}$, $\delta_{\text{Cr, cavity-cluster}}$, and $\delta_{\text{Cr detached particles}}$ values were 8%–21%, 7%–21%, 8%–27%, and >96%, respectively.

4. Discussion

4.1. Effects of Ni^{2+} ion reduction during the anodic dissolution of Inconel 600

At a fixed Fe content, the Ni content in the salts decreased with increasing Cr content, whereas the Cr content decreased sharply across the thickness direction of the Inconel 600 immersed in the LiCl–KCl–5-wt.%-$NiCl_2$ molten salts after the NI-1 and NI-2 experiments (Table 2). This indicates that the highly reducing Cr in Inconel 600 reacted with the less-reactive Ni^{2+} ion, whereas Fe did not, despite possessing a lower standard electrochemical potential. The following chemical reaction occurred in the Inconel 600 immersed in the LiCl–KCl–$NiCl_2$ molten salt.

$$\mathrm{Ni^{2+} + Cr \rightarrow Ni + Cr^{2+}} \qquad (3)$$

As illustrated in Fig. 3 (a-1, a-2, b-1, and b-2), the Ni-coated layers of NI-1 and NI-2 were approximately 3 μm thick; however, that of NI-2 was significantly denser than that of NI-1. This indicates that the reaction between Ni^{2+} and Cr in Inconel 600 was aggressive, until the formation of a compact reduced Ni layer that disturbed the reaction. Thus, electroless plating by the reduced Ni film coating on the surface of Inconel 600 occurred when it was immersed in the molten LiCl–KCl–$NiCl_2$ additive, via the reaction between Ni^{2+} and Cr.

The formation of the Cr–Fe depletion layer was the major characteristic of the anodic dissolution of Inconel 600, with the LiCl–KCl–$NiCl_2$ additive as the electrolyte. The applied potentials and current densities for the anode during the NP and NG experiments were set not to reduce Ni^{2+} ions in the molten salt. A sufficiently large cathode area was provided to allow for a similar environment for the molten salt-based decontamination process and to analyse the dissolved amount of Cr and Fe at the anode qualitatively. It was confirmed that high-purity Ni (>99%) with Cr and Fe concentrations less than 0.0010 wt.% was recovered at the cathode. The Cr and Fe in the Inconel 600 continuously dissolved and accumulated in the molten salt during the anodic dissolution experiment. From the maximum contents of Cr or Fe in the molten salt (Table 4: NG-1 and NP-1), the cathode potential for their facile reduction was calculated using the Nernst equation. The E_{eq} values were calculated as −0.339 and −0.113 V (vs. Ag/1 wt.% AgCl) for Cr and Fe, respectively, although the activity of each element in the reduced metal at the cathode had been set to 0.001 to assume the very reductive condition. These potentials were lower than the cathode potential during the experiment (Fig. 4) which implies that the reduction of Cr and Fe did not occur during the experiments.

The thickness of the Cr–Fe depletion layer and the remaining Ni content decreased, and the amount of Cr and Fe remaining in the layer increased with the potential or current density. The expected formation mechanism is illustrated in Fig. 10. Although electrochemical dissolution weakened the structural integrity of Inconel 600 (Fig. 10 (a)), the reduced Ni generated by the chemical reaction with Cr compensated for the damage (Fig. 10 (c)), and a reinforced region that dissolved the remaining Cr and Fe appeared as a Cr–Fe depletion layer (Fig. 10 (d)). Because the rates of dissolution of the Cr and Fe in the Inconel 600 increased with the applied potential or current density and the rate of the chemical reaction supplementing the structural integrity remained unchanged, structural disruption was accelerated at a higher applied potential or current density. Essentially, low Cr and Fe dissolution rates provided sufficient time for the chemical reaction and facilitated the formation of a thicker Cr–Fe depletion layer. A high Cr and Fe dissolution rate reduced the time for the reinforcing reaction, which split the Cr–Fe depletion layer, although dissolvable Cr and Fe still remained.

The reduced thickness of the anode was significantly larger than the thickness of the Cr–Fe depletion layer, indicating that the layer detachment produced detached particles during anodic dissolution. The detached particles, whose compositions are listed in Table 7, also exhibited the same behaviour. The remaining Cr and Fe contents in the detached particles were higher under higher-current-density conditions than under lower-current-density conditions. The sizes of the detached particles decreased with increasing current density, indicating that early detachment occurred during Cr–Fe depletion layer growth at higher current densities.

As shown in Fig. 4, the anodic current density decreased continuously during the NP experiment, and the current densities for NP-1, NP-2, and NP-3 at the final stage were reduced by 53.3%, 70.8%, and 86.9%, respectively, compared to their current densities at the initial stage. This phenomenon was caused by the reduced Cr and Fe contents in the Cr–Fe depletion layer and a reduced current density decrement rate caused by a thinner Cr–Fe depletion layer and higher Cr and Fe contents therein, as reported in Table 3. After the NP experiments, the salt compositions were found to change. The degree of increase of the Cr content decreased with increasing applied potential. The Fe content showed the opposite trend; however, it was hard to analyse quantitatively because of the complex relationship between the electrochemical dissolution of Cr, Fe, and Ni in Inconel 600 and the chemical reaction between Ni^{2+}/Cr in the anode and the detached particles. The noise in the current density response is expected to be occurred because the Cr–Fe depletion layer interferes with the smooth dissolution of the alloying elements.

In the NG experiments, the anode potential increased sharply during the first 5 min and then increased gradually, because the Cr–Fe depletion layer, with low Cr and Fe contents, disturbed Cr and Fe dissolution. Under similar conditions, the measured anode potential of the NG experiments was higher than the applied potential of the NP experiments, which is can be explained by the high Fe content that has a higher redox potential than Cr, in the molten salt (Table 4).

4.2. Growth behaviour of the cavity-cluster layer according to the applied potential and current density

The Cr and Fe content changes were negligible in the FI-1 experiment, in which the Inconel 600 specimen was immersed in the LiCl–KCl–5-wt.%-$FeCl_2$ molten salt for 168 h (Table 2). The reaction between Fe^{2+} and Cr in Inconel 600 was very slow because the redox-potential difference between Cr and Fe is low. The anodic dissolution behaviour of Inconel 600 in the LiCl–KCl–5-wt.%-$FeCl_2$ molten salt was different from that in the $NiCl_2$ additive salt, owing to the inactive Fe^{2+} ion. A cavity-cluster layer, with several microcavities on its surface, was observed after the potentiostatic or galvanostatic anodic dissolution.

In the FP and FG experiments, the applied potential or current density was set such that the Fe^{2+} ion was not reduced at the anode. The reduced metal at the cathode was characterised by a Ni content of <0.0050 wt.%. Furthermore, the Ni content in the salt after the experiments (Table 6) implied that a small amount of Ni had dissolved but most of it had been captured at the cathode. Thus, the effect of Ni^{2+} ion reduction on the Inconel 600 which can reinforce the structural integrity of the specimen during the anodic dissolution could be neglected. E_{eq} for Cr was −0.3756 V (vs. Ag/1 wt.% AgCl) under the salt condition of Table 6 FP-2 which takes the largest Cr content and that of activity in the deposit had been set to 0.001, which was more negative than the measured cathode potential. The Cr content in the reduced metal also indicated insignificant Cr reduction.

As shown in Fig. 8, which presents the microstructure of the FP-4 and FG-4 experiments, when a small charge (1 C cm^{-2}) was passed under anodic dissolution conditions of 0.05 V (vs. Ag/1 wt.% AgCl) and 6 mA cm^{-2}, different surface dissolution behaviours were observed, depending on the electrochemical dissolution methods. Very narrow but deep cracks were formed on the surface after the FP-4 experiment, whereas wide and relatively shallow cracks were formed after the FG-4 experiment. This tendency was also confirmed by an FP-1 χ value, which was significantly larger than that of FG-1 (Table 6), indicating that a higher amount of Fe had been dissolved, along with more significant crack formation, under the galvanostatic condition compared to the potentiostatic condition. Furthermore, as shown in Fig. 6, the anode potential of FG-1 was 60 mV higher than the applied potential of FP-1, indicating that a higher amount of Fe had been dissolved, which caused the microstructural change.

In the FP experiments, the χ value continuously decreased as the applied potential increased. Sharp crevices, with definite borders, were generated at lower applied potentials or the higher χ values (FP-1 and FP-2), whereas rough crevices, which appeared to be peeled, were formed at higher applied potentials or lower χ values (FP-3). Under similar conditions, the χ value of FG was less than half that of FP, with anode potentials 60–120 mV higher than the applied potentials of the FP experiments. These results also explained the effect of local Fe dissolution on Inconel 600. δ_{Cr} of the detached particles was >96%, irrespective of the applied current density, whereas δ_{Fe} was 6.95% for FG-1 and 21.01% for FG-3. This indicates that the detachment of granules started with the exhaustion of Cr and an increase in the Fe dissolution rate with the applied current density.

Based on these discussions, the anodic dissolution behaviours of Inconel 600 in molten LiCl-KCl-$FeCl_2$ salt are described in Fig. 11. The Inconel 600 in LiCl-KCl-$FeCl_2$ salt (Fig. 11 (a)) dissolves its alloying elements at its grain boundaries and its surface which are usually considered as the rapid diffusion channel for alloy elements (Fig. 11 (b)). Comparing the anode potential and salt composition change of the potentiostatic experiments and galvanostatic experiments, the dissolution of Fe in Inconel 600 is more limited under potentiostatic conditions. When the applied potential is fixed, Cr which is the most reactive element dissolves through the grain boundary and a small amount of Fe which is less reactive can dissolve into the molten salt (Fig. 11 (c)). After sufficient anodic dissolution through the grain boundary occurs, the remaining grain leaves from the anode (Fig. 11 (d)). Meanwhile, under the galvanostatic condition, a larger amount of Fe was dissolved into the molten salt relative to the potentiostatic condition. This indicates that the cracks can be broadened because of the Cr and Fe dissolution (Fig. 11 (e)). The remaining grain will be detached from the anode when the grain boundaries that can hold the grain are dissolved (Fig. 11 (f)).

It is expected that the difference in the anodic dissolution behaviour is caused by different factors limited by each applied electrochemical method. The potential of Inconel 600 is strictly fixed by applying the potentiostatic condition, and it is possible to allow the Cr dissolution, whereas Fe dissolution is limited by applying a certain level of potential. Therefore, cracks that occurred because of potentiostatic dissolution penetrate deeply into the specimen, to melt Cr, and cause a grain boundary attack. On the other hand, the anode potential is changeable when a galvanostatic condition is applied. Thus, Fe dissolves along the interface between the anode and molten salt rather than thoroughly dissolving the Cr inside the specimen. For this reason, the anode potential of the galvanostatic experiments was higher and the χ value (Table 6) was lower despite the similar level of current density applied in the potentiostatic experiments. Further, the angularity of the cavity-cluster layer decreased as the potential increases.

5. Conclusion

The anodic dissolution behaviours of Inconel 600 in LiCl–KCl–5 wt.% $NiCl_2$/$FeCl_2$ were investigated at 773 K. In the system with the $NiCl_2$ additive, Cr and Fe can be eliminated selectively from Inconel 600 via the formation of a Cr–Fe depletion layer during the anodic dissolution process, and a significant fraction of Cr or Fe can be dissolved in molten salts by applying a low current density. The chemical reduction reaction of the Ni^{2+} ion on the Inconel 600 could explain the Cr–Fe depletion layer generation mechanism.

The cavity-cluster layer was generated by applying the oxidative condition to Inconel 600 in a LiCl–KCl–5 wt.% $FeCl_2$ system. The dissolution of Cr and Fe in Inconel 600 occurs and develops through its grain boundaries, and this results in the detachment of the remaining grain from the anode. The microstructural changes with respect to applied electrochemical conditions were analysed, and the anode potential condition is considered a major factor that affects the degree of angularity in the cavity-cluster layer.

Declaration of competing interest

The authors declare that they have no known competing financial interests or personal relationships that could influence the study reported in this paper.

Data availability

The raw/processed data required to reproduce these findings cannot be shared at this time as the data also forms part of an ongoing study.

Acknowledgments

This study was supported by a National Research Foundation of Korea (NRF) grant funded by the Ministry of Science and ICT, Republic of Korea (NRF-2022M2D2A1A02063129).

References

[1] A. Ayodeji, Y.-k. Liu, PWR heat exchanger tube defects: Trends, signatures and diagnostic techniques, Prog. Nucl. Energy. 112 (2019) 171–184. https://doi.org/10.1016/j.pnucene.2018.12.017.

[2] G. Bertali, F. Scenini, M.G. Burke, Advanced microstructural characterization of the intergranular oxidation of Alloy 600, Corros. Sci. 100 (2015) 474–483. https://doi.org/10.1016/j.corsci.2015.08.010.

[3] S.M. Bruemmer, L.A. Charlot, C.H. Henager Jr, Microstructure and microdeformation effects on IGSCC of Alloy 600 steam generator tubing, Corrosion. 44 (1988) 782–788. https://doi.org/10.5006/1.3584948.

[4] D. Cao, Z. Shi, D. Shi, J. Xu, X. Hu, Z. Wang, Electrochemical oxidation of Fe–Ni alloys in cryolite–alumina molten salts at high temperature, J. Electrochem. Soc. 166 (2019) E87–E96. https://doi.org/10.1149/2.0501904jes.

[5] J. Cavaghan, Decontamination and recovery of a nuclear facility to allow continued operation, Radiat. Prot. Dosimetry. 173 (2017) 118–123. https://doi.org/10.1093/rpd/ncw296.

[6] Y. Çetin, A. Acır, Simulating the erosion modelling of pipes used in nuclear power plants in terms of physical decontamination, Prog. Nucl. Energy. 150 (2022) 104284. https://doi.org/10.1016/j.pnucene.2022.104284.

[7] W.-S. Choi, S.-H. Cho, Y.-J. Lee, Y.-S. Kim, J.-H. Lee, Separation behavior of nickel and cobalt in a LiCl-KCl-$NiCl_2$ molten salt by electrorefining process, J. Electroanal. Chem. 866 (2020) 114175. https://doi.org/10.1016/j.jelechem.2020.114175.

[8] D.R. Diercks, W.J. Shack, J. Muscara, Overview of steam generator tube degradation and integrity issues, Nucl. Eng. Des. 194 (1999) 19–30. https://doi.org/10.1016/S0029-5493(99)00167-3.

[9] A.S. Dorcheh, R.N. Durham, M.C. Galetz, Corrosion behavior of stainless and low-chromium steels and IN625 in molten nitrate salts at 600 °C, Sol. Energy Mater. Sol. Cells. 144 (2016) 109–116. https://doi.org/10.1016/J.SOLMAT.2015.08.011.

[10] R.S. Dutta, Corrosion aspects of Ni–Cr–Fe based and Ni–Cu based steam generator tube materials, J. Nucl. Mater. 393 (2009) 343–349. https://doi.org/10.1016/j.jnucmat.2009.06.020.

[11] J.C. Gomez-Vidal, R. Tirawat, Corrosion of alloys in a chloride molten salt (NaCl-LiCl) for solar thermal technologies, Sol. Energy Mater. Sol. Cells. 157 (2016) 234–244. https://doi.org/10.1016/J.SOLMAT.2016.05.052.

[12] M. Hofmeister, L. Klein, H. Miran, R. Rettig, S. Virtanen, R.F. Singer, Corrosion behaviour of stainless steels and a single crystal superalloy in a ternary LiCl−KCl−CsCl molten salt, Corros. Sci. 90 (2015) 46–53. https://doi.org/10.1016/j.corsci.2014.09.009.

[13] M. Hornáček, V. Nečas, Assessment of the radiation impact of steam generator dismantling on the workers, public and environment, Prog. Nucl. Energy. 91 (2016) 345–354. https://doi.org/10.1016/j.pnucene.2016.05.003.

[14] M. Hornáček, V. Nečas, The analysis of management of radioactive waste arisen from steam generator's dismantling from radiological and economical point of view, Prog. Nucl. Energy. 100 (2017) 406–418. https://doi.org/10.1016/J.PNUCENE.2017.07.007.

[15] H. Ocken, Decontamination Handbook, EPRI Report TR-112352, 1999.

[16] J.-H. Park, S.-Y. Cho, J.-J. Kim, K. Kim, Y. Bang, Study of transient events during the full-system chemical decontamination operation of the Kori-1 nuclear power plant, Ann. Nucl. Energy. 174 (2022) 109164. https://doi.org/10.1016/j.anucene.2022.109164.

[17] V. Kumar, R. Goel, R. Chawla, M. Silambarasan, R.K. Sharma, Chemical, biological, radiological, and nuclear decontamination: Recent trends and future perspective, J. Pharm. Bioallied Sci. 2 (2010) 220–238. https://doi.org/10.4103/0975-7406.68505.

[18] B.A. Gusev, I.S. Orlenkov, L.N. Moskvin, N.G. Sandler, A.A. Efimov, AM. Aleshin, V.V. Krivobokov, V.N. Vavilkin, Experience in decontamination of naval reactor plants, Nucl. Technol. 206 (2020) 791–803. https://doi.org/10.1080/00295450.2019.1693216.

[19] S.S. Hwang, H.P. Kim, SCC analysis of Alloy 600 tubes from a retired steam generator, J. Nucl. Mater. 440 (2013) 129–135. https://doi.org/10.1016/j.jnucmat.2013.04.061.

[20] S.S. Hwang, H.P. Kim, J.S. Kim, K.E. Kasza, J. Park, W.J. Shack, Leak behavior of SCC degraded steam generator tubings of nuclear power plant, Nucl. Eng. Des. 235 (2005) 2477–2484. https://doi.org/10.1016/j.nucengdes.2005.06.013.

[21] G.-N. Kim, M.-W. Lee, H.-M. Park, W.-K. Choi, K.-W. Lee, Abrasive blasting technology for decontamination of the inner surface of steam generator tubes, Nucl. Eng. Technol. 43 (2011) 469–476. https://doi.org/10.5516/NET.2011.43.5.469.

[22] U.C. Kim, K.M. Kim, E.H. Lee, Effects of chemical compounds on the stress corrosion cracking of steam generator tubing materials in a caustic solution, J. Nucl. Mater. 341 (2005) 169–174. https://doi.org/10.1016/j.jnucmat.2005.01.018.

[23] C.H. Lee, K.H. Kang, M.K. Jeon, C.M. Heo, Y.L. Lee, Electrorefining of zirconium from zircaloy-4 cladding hulls in LiCl-KCl molten salts, J. Electrochem. Soc. 159 (2012)

D463–D468. https://doi.org/10.1149/2.012208jes.

[24] S. Liu, Y. He, H. Xie, Y. Ge, Y. Lin, Z. Yao, M. Jin, J. Liu, X. Chen, Y. Sun, B. Wang, A state-of-the-art review of radioactive decontamination technologies: Facing the upcoming wave of decommissioning and dismantling of nuclear facilities, Sustainability. 14 (2022) 4021. https://doi.org/10.3390/su14074021.

[25] J. Hur, S. Jeong, S. Sohn, J. Park, I.S. Hwang, Separation of Zr from Zr-2.5Nb by electrorefining in LiCl-KCl for volumetric decontamination of CANDU pressure tube, Appl. Sci. 11 (2021) 3790. https://doi.org/10.3390/app11093790.

[26] K.T. Park, T.H. Lee, N.C. Jo, H.H. Nersisyan, B.S. Chun, H.H. Lee, J.H. Lee, Purification of nuclear grade Zr scrap as the high purity dense Zr deposits from Zirlo scrap by electrorefining in LiF−KF−ZrF4 molten fluorides, J. Nucl. Mater. 436 (2013) 130–138. https://doi.org/10.1016/j.jnucmat.2013.01.310.

[27] Y.-Z. Cho, T.-K. Lee, H.-C. Eun, J.-H. Choi, I.-T. Kim, G.-I. Park, Purification of used eutectic (LiCl−KCl) salt electrolyte from pyroprocessing, J. Nucl. Mater. 437 (2013) 47–54. https://doi.org/10.1016/j.jnucmat.2013.01.344.

[28] M. Shim, H.-G. Choi, J.-H. Choi, K.-W. Yi, J.-H. Lee, Separation of Cs and Sr from LiCl-KCl eutectic salt via a zone-refining process for pyroprocessing waste salt minimization, J. Nucl. Mater. 491 (2017) 9–17. https://doi.org/10.1016/j.jnucmat.2017.04.036.

[29] M.F. Simpson, T.-S. Yoo, D. Labrier, M. Lineberry, M. Shaltry, S. Phongikaroon, Selective reduction of active metal chlorides from molten LiCl-KCl using lithium drawdown, Nucl. Eng. Technol. 44 (2012) 767–772. https://doi.org/10.5516/NET.06.2011.010.

[30] B. Mishra, D.L. Olson, Molten salt applications in materials processing, J. Phys. Chem. Solids. 66 (2005) 396–401. https://doi.org/10.1016/j.jpcs.2004.06.049.

[31] B. Ooms, I. Verwaest, F. Legee, J.-G. Nokhamzon, M. Pieraccini, P. Poncet, N. Franzen, T. Vignaroli, B. Herschend, T. Benest, Recycling and Reuse of Materials Arising from the Decommissioning of Nuclear Facilities. A Report by the NEA Cooperative Program on Decommissioning, in: Radioactive Waste Management, Organization for Economic Co-operation and Development Publishing, Paris, National Environment Agency – Singapore, 2017.

[32] J. Porcayo-Calderon, O. Sotelo-Mazon, V. Salinas-Bravo, C. Arrieta-Gonzalez, J. Ramos-Hernandez, C. Cuevas-Arteaga, Electrochemical performance of Ni20Cr coatings applied by combustion powder spray in $ZnCl_2$-KCl molten salts, Int. J. Electrochem. Sci. 7 (2012) 1134–1148.

[33] C.J. Rao, P. Venkatesh, S. Ningshen, Corrosion assessment of 9Cr-1Mo steel in molten LiCl-KCl eutectic salt by electrochemical methods, J. Nucl. Mater. 514 (2019) 114–122. https://doi.org/10.1016/j.jnucmat.2018.11.014.

[34] M. Sarvghad, T.A. Steinberg, G. Will, Corrosion of stainless steel 316 in eutectic molten salts for thermal energy storage, Sol. Energy. 172 (2018) 198–203. https://doi.org/10.1016/J.SOLENER.2018.03.053.

[35] H.-W. Seo, D.-H. Lee, D.S. Kessel, C.-L. Kim, Proposal for the management strategy of metallic waste from the decommissioning of Kori Unit 1 by using melting and segmentation technology, Ann. Nucl. Energy. 110 (2017) 633–647. https://doi.org/10.1016/j.anucene.2017.06.056.

[36] Z. Shen, K. Arioka, S. Lozano-Perez, A mechanistic study of SCC in Alloy 600 through high-resolution characterization, Corros. Sci. 132 (2018) 244–259. https://doi.org/10.1016/J.CORSCI.2018.01.004.

[37] Z. Shen, K. Chen, D. Tweddle, G. He, K. Arioka, S. Lozano-Perez, Characterization of the crack initiation and propagation in Alloy 600 with a cold-worked surface, Corros. Sci. 152 (2019) 82–92. https://doi.org/10.1016/J.CORSCI.2019.03.014.

[38] A. Szabó, K. Varga, Z. Németh, K. Radó, D. Oravetz, K.É Makó, Z. Homonnay, E. Kuzmann, P. Tilky, J. Schunk, G. Patek, Effect of a chemical decontamination procedure on the corrosion state of the heat exchanger tubes of steam generators, Corros. Sci. 48 (2006) 2727–2749. https://doi.org/10.1016/j.corsci.2005.09.008.

[39] S. Yoon, S. Choi, Spectroelectrochemical behavior of Cr, Fe, Co, and Ni in LiCl-KCl molten salt for decontaminating radioactive metallic wastes, J. Electrochem. Soc. 168 (2021) 013504. https://doi.org/10.1149/1945-7111/abdc7e.

[40] L. Zhong, J. Lei, J. Deng, Z. Lei, L. Lei, X. Xu, Existing and potential decontamination methods for radioactively contaminated metals-A Review, Prog. Nucl. Energy. 139 (2021) 103854. https://doi.org/10.1016/j.pnucene.2021.103854.

[41] M. Zhu, S. Zeng, H. Zhang, J. Li, B. Cao, Electrochemical study on the corrosion behaviors of 316 SS in HITEC molten salt at different temperatures, Sol. Energy Mater. Sol. Cells. 186 (2018) 200–207. https://doi.org/10.1016/J.SOLMAT.2018.06.044.

[42] T.-J. Zhu, W. Huang, Q.-N. Li, Electrorefining of nickel from nickel–chromium alloy in molten LiCl−KCl, Nucl. Sci. Tech. 30 (2019) 1–8. https://doi.org/10.1007/s41365-019-0656-5.

Figure Captions

Fig. 1. Schematics of the electrochemical cell, reference electrode, and anode.

Fig. 2. Schematic of the microparticle-recovery system.

Fig. 3. Microstructures of the Inconel 600 specimens immersed in the LiCl–KCl–5-wt.%-$NiCl_2$ molten salt for 3 (a-1) and 168 h (b-1) and those of Inconel 600 specimens immersed in the LiCl–KCl–5-wt.%-$FeCl_2$ molten salt for 168 h (c). The compositions across the thickness direction of the deposited layer (a-2 and b-2, EDS point analyses were conducted along the dashed purple line).

Fig. 4. Chronoamperograms of the NP-1, NP-2, and NP-3 experiments (a, b, and c) and chronopotentiograms of the NG-1, NG-2, and NG-3 (d, e, and f) experiments.

Fig. 5. Microstructures of Inconel 600 after the NP and NG experiments: NP-1, NP-2, and NP-3 (a, b, and c) and NG-1, NG-2, and NG-3 (d, e, and f).

Fig. 6. Chronoamperograms of the FP-1, FP-2, and FP-3 experiments (a, b, and c) and chronopotentiograms of the FG-1, FG-2, and FG-3 (d, e, and f) experiments.

Fig. 7. Microstructures of Inconel 600 after the FP and FG experiments: FP-1, FP-2, and FP-3 (a, b, and c) and FG-1, FG-2, and FG-3 (d, e, and f).

Fig. 8. Microstructure of Inconel 600 and its expanded image after the FP-4 (a-1 and a-2) and FG-4 (b-1, b-2) experiments.

Fig. 9. SEM–EDS images of detached particles collected using a microparticle-recovery system after the anodic dissolution experiments in NG-1 (a), NG-3 (b), FG-1 (c), and FG-3 (d).

Fig. 10. Schematics of Cr–Fe depletion layer formation mechanism: initial stage of the Inconel 600 and the molten salt (a), ionisation of Cr and Fe due to applied potential or current density (b), Ni reduction due to chemical reaction between Ni^{2+} ion in molten salt and Cr in Inconel 600 on the position where the alloying elements are dissolved (c), and Cr–Fe depletion layer growth which ensure the dissolution of remaining elements in Inconel 600 (d).

Fig. 11. Schematics of anodic dissolution behaviours of Inconel 600 in molten LiCl–KCl–$FeCl_2$ salt with potentiostatic method (a–d) and galvanostatic method (a, b, e, f).

Tables

Table 1. Corrosion test and anodic dissolution via the potentiostatic and galvanostatic methods in LiCl–KCl–5-wt.%-$NiCl_2$/$FeCl_2$.

Test ID	Applied method	Applied potential (V vs. 1 wt.% Ag/AgCl)	Applied current density (mA cm^{-2})	Note
NI-1	Immersion test	-	-	3 h
NI-2		-	-	168 h
FI-1		-	-	168 h
NP-1	Potentiostatic	+0.15		287 C cm^{-2} (1,000 C)
NP-2		+0.20		
NP-3		+0.25		
NG-1	Galvanostatic		+6	
NG-2			+16	
NG-3			+30	
FP-1	Potentiostatic	+0.05		80 C cm^{-2} (280 C)
FP-2		+0.10		
FP-3		+0.15		
FP-4		+0.05		1 C cm^{-2} (3.5 C)
FG-1	Galvanostatic		+6	80 C cm^{-2} (280 C)
FG-2			+16	
FG-3			+30	
FG-4			+6	1 C cm^{-2} (3.5 C)

N, $NiCl_2$ additive salt; F, $FeCl_2$ additive salt; I, immersion test; P, anodic dissolution via the potentiostatic method; G, anodic dissolution via the galvanostatic method.

Table 2. Contents of the major elements in the molten salts before and after the NI-1, NI-2, and FI-1 experiments, as determined via ICP–OES.

	Elemental contents in the salt (wt.%)		
	Ni [$NiCl_2$]	Fe [$FeCl_2$]	Cr [$CrCl_2$]
Before the NI experiment	2.2735 [5.0201]	0.0023 [0.0052]	0.0017 [0.0040]
NI-1 (3 h)	2.2439 [4.9547]	0.0044 [0.0100]	0.0233 [0.0551]
NI-2 (168 h)	2.2184 [4.8984]	0.0032 [0.0073]	0.0632 [0.1494]
Before the FI experiment	0.0011 [0.0024]	2.2213 [5.0417]	0.0048 [0.0113]
FI-1 (168 h)	0.0005 [0.0011]	2.2223 [5.0439]	0.0032 [0.0076]

*Values in square brackets are chloride contents calculated with the assumption that whole ions formed the divalent chloride.

Table 3. Characteristics of the specimens and their Cr–Fe depletion layers in the NP and NG experiments.

				Elemental contents in the Cr–Fe depletion layer (wt.%)		
Test ID	Applied condition	Thickness of the Cr–Fe depletion layer (μm)	Reduced thickness of the specimen (μm)	Ni	Fe	Cr
Unreacted specimen	-	-	-	73.73	9.59	16.68
NP-1	0.15 V	~40	~130	95.20	1.72	3.08
NP-2	0.20 V	~30	~150	93.19	2.27	4.54
NP-3	0.25 V	~15	~180	91.02	2.90	6.08
NG-1	6 mA cm^{-2}	~30	~90	99.28	0.34	0.37
NG-2	16 mA cm^{-2}	~20	~110	97.55	1.33	1.12
NG-3	30 mA cm^{-2}	~15	~110	94.00	2.24	3.75

Table 4. Contents of the major elements in the molten salts before and after the NP and NG experiments, as determined via ICP–OES.

		Elemental contents in the salt (wt.%)		
Test ID	Applied condition	Ni [$NiCl_2$]	Fe [$FeCl_2$]	Cr [$CrCl_2$]
Before	-	2.2807 [5.0356]	0.0011 [0.0025]	0.0008 [0.0019]
NP-1	0.15 V	1.2736 [2.8122]	0.2416 [0.5484]	0.6862 [1.6220]
NP-2	0.20 V	1.2675 [2.7987]	0.2645 [0.6003]	0.6724 [1.5893]
NP-3	0.25 V	1.2785 [2.8230]	0.3002 [0.6814]	0.6171 [1.4586]
NG-1	6 mA cm^{-2}	1.2568 [2.7751]	0.3280 [0.7445]	0.6294 [1.4877]
NG-2	16 mA cm^{-2}	1.2678 [2.7994]	0.3038 [0.6895]	0.6393 [1.5111]
NG-3	30 mA cm^{-2}	1.2932 [2.8555]	0.3150 [0.7150]	0.6015 [1.4218]

*Values in square brackets are chloride contents calculated with the assumption that whole ions formed the divalent chloride.

Table 5. Characteristics of the specimens and their cavity-clusters in the FP and FG experiments.

				Elemental content in the cavity-cluster layer (wt.%)		
Test ID	Applied condition	Thickness of the cavity-cluster layer (μm)	Reduced thickness of the specimen (μm)	Ni	Fe	Cr

Unreacted specimen	-	-	-	73.73	9.59	16.68
FP-1	0.05 V	~50	~180	78.32	8.42	13.26
FP-2	0.10 V	~50	~200	77.58	9.21	13.21
FP-3	0.15 V	~30	~250	75.85	9.03	15.12
FG-1	6 mA cm^{-2}	~50	~150	78.83	8.11	13.06
FG-2	16 mA cm^{-2}	~35	~150	76.62	8.88	14.50
FG-3	30 mA cm^{-2}	~20	~180	75.31	9.01	15.68

Table 6. Contents of the major elements in the molten salts before and after the FP and FG experiments, as determined via ICP–OES, and the corresponding χ values.

		Elemental content in the salt (wt.%)			
Test ID	Condition	Ni [$NiCl_2$]	Fe [$FeCl_2$]	Cr [$CrCl_2$]	χ
Before	-	0.0014 [0.0031]	2.2099 [5.0158]	0.0026 [0.0061]	-
FP-1	0.05 V	0.0017 [0.0038]	1.9523 [4.4311]	0.2412 [0.5701]	20.49
FP-2	0.10 V	0.0038 [0.0084]	1.9644 [4.4586]	0.2256 [0.5332]	9.73
FP-3	0.15 V	0.0022 [0.0049]	1.9819 [4.4983]	0.2111 [0.4990]	5.32
FG-1	6 mA cm^{-2}	0.0018 [0.0040]	1.9722 [4.4763]	0.2144 [0.5068]	7.02
FG-2	16 mA cm^{-2}	0.0030 [0.0066]	1.9883 [4.5128]	0.2067 [0.4886]	4.52
FG-3	30 mA cm^{-2}	0.0022 [0.0049]	2.0122 [4.5671]	0.1749 [0.4134]	2.56

Table 7. Sizes and contents of the detached particles shown in Fig. 9.

Specimen number	Size of particle (μm)	Ni (wt.%)	Fe (wt.%)	Cr (wt.%)
	-	73.73	9.59	16.68
NG (6 mA cm^{-2})	20–25	99.46	0.25	0.29
NG (30 mA cm^{-2})	9–12	96.16	1.66	2.18
FG (6 mA cm^{-2})	1–3	88.66	10.73	0.61
FG (30 mA cm^{-2})	1–2	89.93	9.24	0.83

Fig 1.

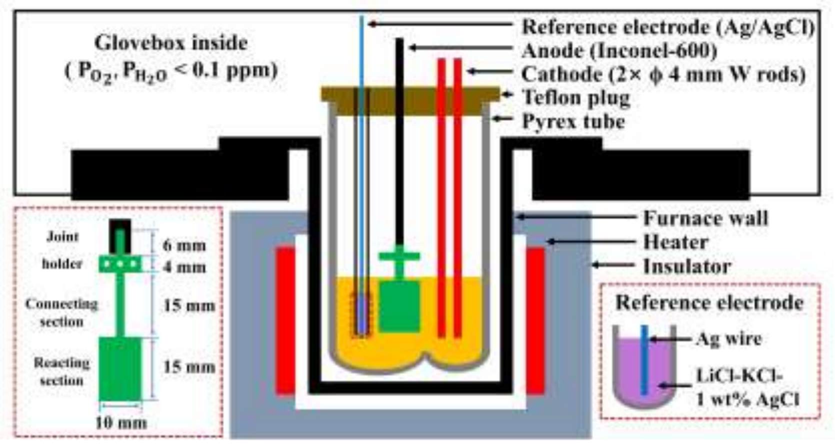

Fig 2

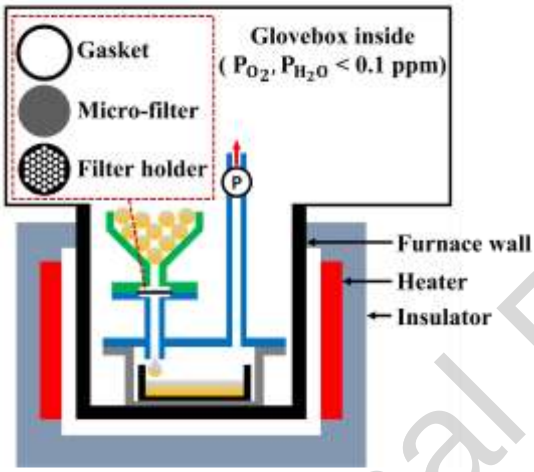

Fig 3

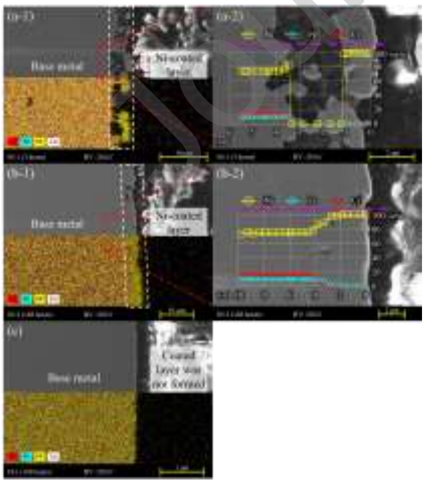

Fig 4

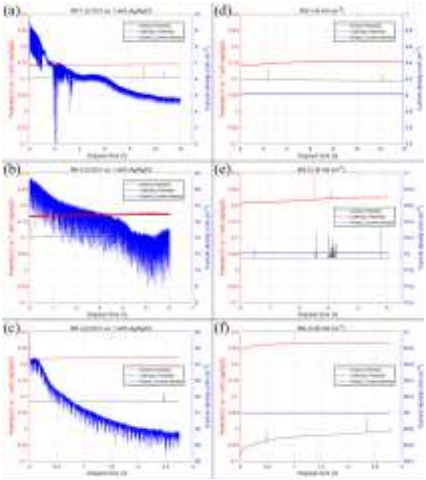

Fig 5

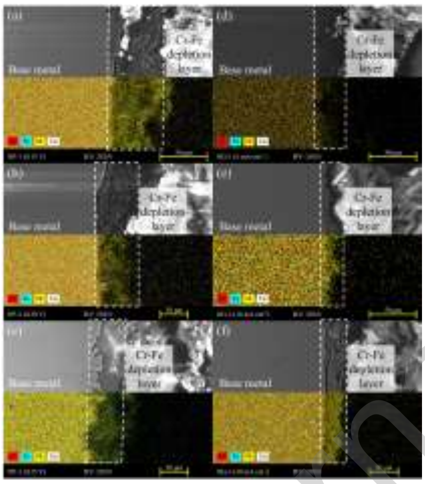

Fig 6

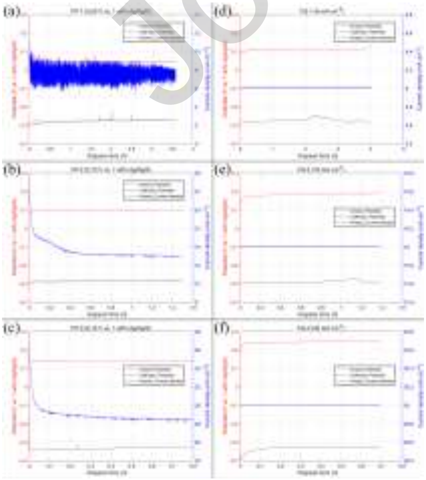

Fig 7

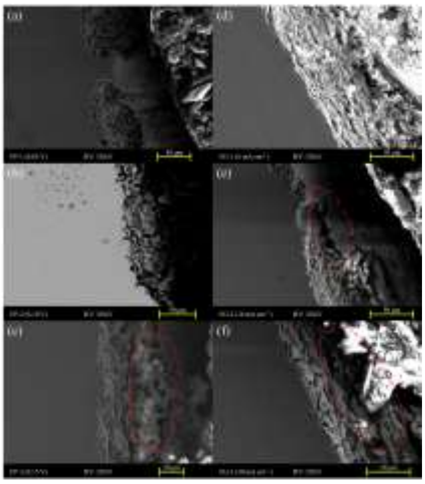
(a)
(d)
(b)
(e)
(c)
(f)

Fig 8

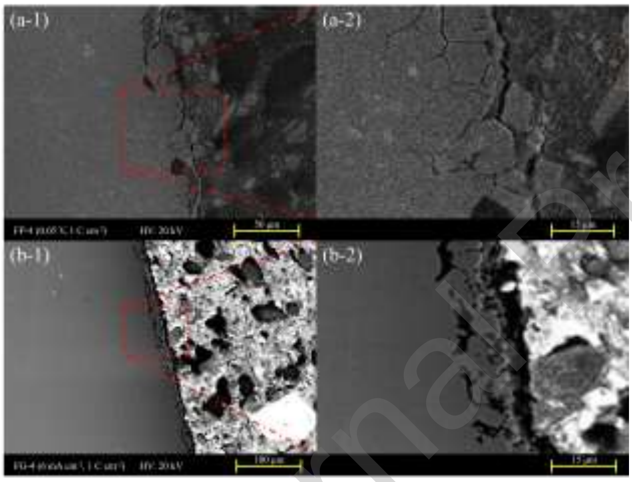
(a-1)
(a-2)
(b-1)
(b-2)
FP-4
HV: 20 kV
50 μm
15 μm
FG-4
HV: 20 kV
100 μm
15 μm

Fig 9

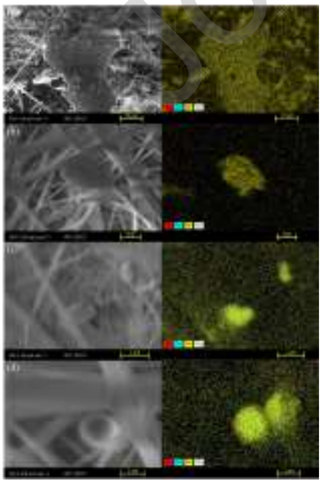
(b)
(d)

Fig 10

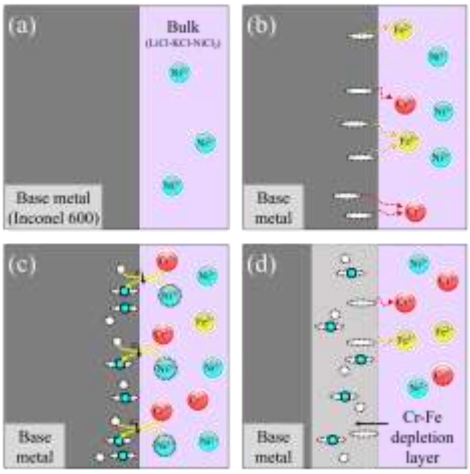

Fig 11

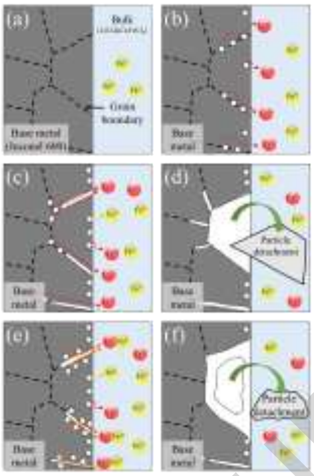

Graphical abstract

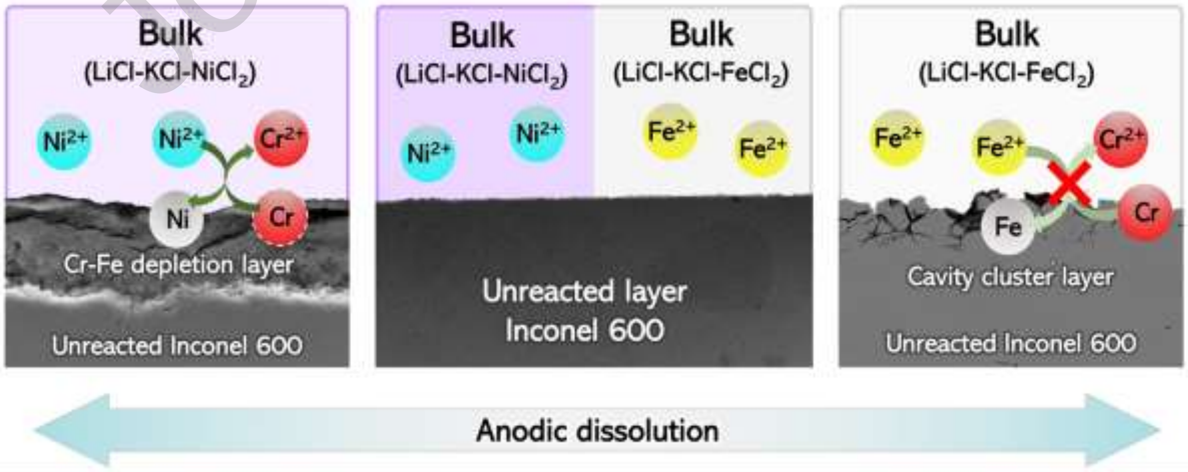

CRediT authorship contribution statement

Younghwan Jeon: Conceptualization, Methodology, Software, Validation, Formal analysis, Investigation, Writing – original draft, Writing – Review & Editing

Jungho Hur: Validation, Formal analysis, Investigation, Resources

Gwan Yoon Jeong: Methodology, Software, Formal analysis, Investigation, Supervision

Seungmin Ohk: Investigation, Resources

Jaeyeong Park: Conceptualization, Methodology, Formal analysis, Writing – original draft, Writing – Review & Editing, Project administration, Funding acquisition

Declaration of interests

☐ The authors declare that they have no known competing financial interests or personal relationships that could have appeared to influence the work reported in this paper.

☒ The authors declare the following financial interests/personal relationships which may be considered as potential competing interests:

Jaeyeong Park reports financial support was provided by National Research Foundation of Korea.

Highlights

- $NiCl_2$ introduces Cr-Fe depletion layer in Inconel 600 during anodic dissolution
- Cr-Fe depletion layer allows continuous Cr and Fe dissolution of Inconel 600
- Inconel 600 with $FeCl_2$ salt suffers grain boundary attack during anodic dissolution
- With $FeCl_2$ salt, Inconel 600 can dissolve Cr selectively by potentiostatic method